Oxidation Behaviour of Ni-Cr-Y_2O_3 Composite Coatings Synthesised by Sol Enhanced Pulse Electroplating

Robert Hoye (Corresponding author)
Department of Chemical and Materials Engineering, The University of Auckland
20 Symonds Street, Private Bag 92019, Auckland 1142, New Zealand
Tel: 64-021-173-9391 E-mail: lzha243@aucklanduni.ac.nz

Wei Gao
Department of Chemical and Materials Engineering, The University of Auckland
20 Symonds Street, Private Bag 92019, Auckland 1142, New Zealand
Tel: 64-099-238-175 E-mail: w.gao@auckland.ac.nz

Received: January 20, 2012 Accepted: February 12, 2012 Published: Apri1 1, 2012
doi:10.5539/jmsr.v1n2p133 URL: http://dx.doi.org/10.5539/jmsr.v1n2p133

Abstract

The objective of this study was to improve the oxidation resistance of electroplated Ni-Cr coatings by introducing a fine dispersion of yttria (Y_2O_3) nanoparticles to the coatings. A technique was developed to produce Y_2O_3 nanoparticles 54 ± 2 nm in size. Electroplating conditions were also investigated and it was found that pulse plating could produce high quality coatings without cracking. The Y_2O_3 nanoparticles were then co-deposited with Ni-Cr and formed a fine dispersion in the coating. The Ni-Cr-Y_2O_3 composite coatings had improved oxidation resistance compared with the conventional Ni-Cr coatings. It is believed that this is due to Y_2O_3 nanoparticles causing finer grains to occur, thereby improving oxide scale adhesion.

Keywords: Nanoparticle synthesis, Oxidation resistance, Pulse electroplating

1. Introduction

By 2035, the world's energy consumption is expected to increase by ~50% from that in 2007 (Doeman, 2010). One important way of improving the efficiency of energy generation and usage is by increasing the high temperature oxidation resistance of materials. According to Carnot's equation, the higher the temperature of the hot reservoir (T_H) compared to that of the cold reservoir (T_0), the higher the thermal efficiency (η) (Smith, Van Ness, & Abbott, 2005). The materials used for high temperature applications, such as Cr-containing steels, have been designed with desirable mechanical properties. However, their limited oxidation resistance restricts them to a maximum service temperature of 700^{o}C (Rahman, Chawla, Jayaganthan, Chandra, & Ambardar, 2010; Trinidade, Christ & Krupp, 2010). If a coating is applied to improve the oxidation resistance, such that the material can operate at 900^{o}C, then the Carnot efficiency increases from approximately 69% to 75% (assuming a T_0 of 25^{o}C). Such efficiency increases can lead to a significant reduction in fuel consumption and CO_2 emissions (Sloof, 2008; Young, 2008).

Oxidation resistance in Ni-Cr coatings is provided by the protective chromia (Cr_2O_3) scale that forms on the surface. However, this scale has a tendency to crack and spall due to growth and thermal stresses. The thermal stress is due to the different thermal expansion of the oxide to the underlying coating and substrate (Sloof, 2008; Wang, Wang, Yu, Zhu, 2008). Previous studies have found that scale adhesion can be improved by the addition of small quantities of rare earth elements, such as yttrium, or their corresponding compounds. This is known as the rare earth effect (Buscail, *et al.*, 2004; Hussey & Graham, 1996; Wang, *et al.*, 2008). One of the theories to explain the rare earth effect is that oxides of rare earth elements act as nucleation sites, causing smaller grains to occur in the oxide scale. The rare earth oxides can also segregate to grain boundaries in the oxide scale and prevent the grains from growing too large in size (Whittle & Stringer, 1980). In either case, it is expected that these effects can be enhanced by adding the rare earths to the coatings as a fine dispersion of nanoparticle

oxides, rather than as an element. This is because the fine dispersion would increase the density of nucleation sites or the number of particles available for pinning grain boundaries. If added as an element, the size and agglomeration of the rare earth oxide particles produced during oxidation could not be controlled.

Electroplated coatings do not need expensive equipment and are therefore much more cost-effective than physical or chemical vapour deposition methods (Gao, 2011). However, when solid nanoparticles are added to electroplating solutions, the particles are typically agglomerated. These agglomerates cannot be broken down by agitation or surfactants effectively. It is therefore difficult to fabricate composite coatings with a real nano-dispersion of particles. But this has recently been accomplished with Ni-TiO_2 composite coatings. This involved developing a method of adding TiO_2 nanoparticles (~10 nm) in the form of sol and co-deposited with Ni or other metals (Chen & Gao, 2010). For this project, this technique was extended to produce yttria (Y_2O_3) nanoparticles for Ni-Cr-Y_2O_3 composite coatings. While there are a number of elements that produce the rare earth effect, yttria was selected as a starting point to determine whether or not the oxidation resistance of electroplated coatings can be improved by adding in rare earth oxides as nanoparticles, rather than as an element in solution.

The hypothesis of this study was that if Y_2O_3 nanoparticles are synthesised in sol and added to the electrolyte of Ni-Cr to produce Ni-Cr-Y_2O_3 composite coatings, then the oxidation resistance is greater than if the Y was added as an element or agglomerated oxide particles. To test this hypothesis there were three specific aims. The first was to develop a repeatable method for synthesising Y_2O_3 nanoparticles in sol. The second aim was to develop the electroplating process to deposit Ni-Cr coatings with good oxidation and wear resistance. The third aim was to compare the oxidation resistance of Ni-Cr coatings electroplated from electrolytes that had Y element, Y_2O_3 powder and Y_2O_3 sol added.

2. Experimental Procedure

The method for synthesising nanoparticles of Y_2O_3 in sol was developed to fulfil the first aim of this project and is discussed in Section 3.1. The final method used was to add 9 mL of 1 mol/L NaOH dropwise at 0.1 mL/min to 40 mL of 1.8 mol/L Y^{3+} solution under 600 rpm magnetic stirring. A water bath was used to keep the temperature constant at ~20^{o}C. The sol, containing 0.04 mol/L of Y_2O_3, was added to the electroplating solution discussed in Section 3.2 in place of 49 mL of distilled water. It was necessary to leave this solution at room temperature for two days in order for the Y-O complexes to form Y_2O_3 particles and the Cr^{3+} to complex with glycine. Afterwards, the solution was stored at 4^{o}C to reduce nanoparticle growth to a very low rate.

Transmission electron microscopy (TEM) was used to characterise the nanoparticles formed in the sol. The instrument used was a Philips CM12 microscope with an accelerating voltage of 120 kV. A droplet (<1 μL) of Y_2O_3 sol was put onto a copper mesh grid and dried at 40^{o}C for 10 minutes.

The substrates for electroplating were 8 mm by 15 mm rectangular 316 stainless steel samples. These were ground with SiC paper to P1200 grit and cleaned in ethanol. They were then degreased by immersion in xylene for 30 minutes, followed by pickling for 15 minutes in 30% HCl. In DC plating, the current required was set on the power supply. In pulse plating, the forward and reverse currents and pulse durations were set. The pH and temperature of the electrolyte were also controlled at 2.5 and 25^{o}C respectively.

Oxidation testing was performed at 900^{o}C (see Section 1.) in a vertical oxidation furnace. Six quartz crucibles were used to contain the samples and spalled oxides. For each crucible, the total mass and the mass of the crucible only was measured and recorded. This weighing was repeated after 1, 2, 3, 20, 40, 60, 80, 100, 120, 140, 160, 180 and 200 hours of oxidation. Spallation is the mass that is lost from the coating and was calculated from the change in mass of the crucible over the time of oxidation. The net mass was the difference between the total mass and crucible mass. The change in net mass over the time of oxidation gave the mass gain.

The wear resistance of the electrodeposited coatings was measured using a Nanovea Tribometer. The sample was oscillated linearly at a rate of 100 rpm for 1510 revolutions under a 6 mm diameter alumina ball with a 2 N load applied. The amplitude was set to ~10 mm. Optical microscopy was used to measure the width of the wear tracks, from which the volume loss was calculated.

The surface morphology and cross-sections of the Ni-Cr coatings were analysed using an XL30S FEG scanning electron microscope that was also equipped with an energy dispersive spectroscope (EDS).

X-ray Diffraction was done using a D8 Advance Bruker AXS diffractometer, which used collimated and monochromated Cu-K_α X-rays (λ = 0.15406 nm) produced at 40 kV and 40 mA (Seal, 2011). Diffracted X-rays were collected at scanning angles (2θ) of 40^o to 76^o with a scanning interval of 0.020^o and step time of 1 s. The

peaks from the collected spectra were matched against a library of peaks using DIFFRAC^{plus} to determine the compounds present.

3. Results and Discussion

3.1 Yttria Nanoparticle Synthesis

The yttria nanoparticle synthesis method developed was given in Section 2. Evidence was obtained to determine whether the sol of well-dispersed Y_2O_3 nanoparticles was produced, and the reaction mechanism was studied.

3.1.1 Method for Nanoparticle Synthesis

From the previous work undertaken on the synthesis of nanoparticles in sol, the key feature of successful results was avoiding equilibrium conditions to prevent the particles from growing too large (Gao, 2009). To fulfil this, the solution of Y^{3+} was kept at room temperature using a water bath, and the solution agitated at 600 rpm. The setup used for this controlled hydrolysis and condensation technique is shown in Figure 1 and the method for producing 0.04 mol/L Y_2O_3 sol given in Section 2. It is desirable to maximise the concentration of Y_2O_3 produced, as this is expected to maximise the improvement in oxidation resistance. However, this would require increasing the OH^- concentration. If $[OH^-]$ is too high, then precipitation occurs. From our preliminary experiments, it was found that this was mitigated by reducing the droplet size and addition rate, and by increasing the concentration of Y^{3+}. 0.2 mol/L Y_2O_3 was the most concentrated sol produced in these trials. This was done by adding 6.7 mL of 2.9 mol/L NaOH at 0.1 mL/min to 20 mL of 2.2 mol/L Y^{3+}. However, it was found that the amount of nitric acid needed to solubilise the high concentration of yttria precursor meant that the pH was too low (~0) for uniform Ni-Cr coatings to be produced. Hence, 0.04 mol/L Y_2O_3 sol was used in further investigations.

One of the advantages of producing nanoparticles in sol is that the particles are well dispersed. By contrast, when solid powder is added to water, they tend to agglomerate due to the high surface energy. To show this difference, both yttria sol and a mixture of yttria powder were prepared. The Y_2O_3 sol was colourless, whereas the powder mixed in water was opaque. The opacity would be due to the agglomerates of yttria powder scattering light. For the sol to be colourless, the particles in the original sol must have been well-dispersed in order for the particles to be small enough to not scatter light. This supports the conclusion that the sol contained a dispersion of nanoparticles rather than agglomerates.

To measure the particle size, TEM micrographs were taken of a dried droplet of yttria sol (Figure 2). Image analysis was used to determine the mean equivalent circle diameter of the particles, which was found to be 54 ± 2 nm for the nanoparticles from sol. The agglomeration of particles shown in Figure 2 is due to the drying of the sol.

This shows that well-dispersed nanoparticles of yttria in sol were indeed produced by the technique developed. The technique is advantageous over other sol-gel techniques, which involve precipitating the Y_2O_3 out as a solid powder, invariably leading to their agglomeration (Cheng, 1999).

3.1.2 Mechanism for Nanoparticle Synthesis

For the sol-gel method, when a hydrolysing agent is added to the sol, the sol undergoes hydrolysis and condensation reactions (Barlier, Bounor-Legaré, Boiteux, Davenas, & Léonard, 2008). It is therefore expected that when OH^- is added to Y^{3+} solution, the reactions occur by paths *a* (hydrolysis) and *b* (condensation) of Figure 3. The Y – O complex formed after condensation would complex further with OH^- and Y^{3+} until the atomic ratio of Y to O is 2:3.

The greater the amount of hydroxide added to the Y^{3+} mixture, the more Y_2O_3 nanoparticles that are produced. But if excessive hydroxide is added, then the forward reaction rate along path *c* in Figure 3 would be increased, leading to the precipitation of Y^{3+} as $Y(OH)_3$ and formation of a gel. However, it was found that when OH^- was added dropwise at a rate of 0.1 mL/min, white precipitates initially formed but disappeared with agitation. This would have been because agitation broke apart the precipitates and exposed them to excess Y^{3+}, which would have attracted the OH^- to complex in a similar way to path *a* of Figure 3.

Five experiments were conducted to investigate the veracity of the proposed reaction mechanism. The 'base conditions' were 20 mL of 0.2 mol/L Y^{3+}, 600 rpm agitation, and 50 μL droplets of 0.2 mol/L NaOH added at 0.1 mL/min. All of these variables were changed one at a time, except for the volume of the Y^{3+} solution. From Figures 4 and 6, it can be seen that the droplet rate, droplet size and agitation rate did not significantly change the volume of NaOH added for the sol-gel transition to occur. It can also be seen that the ratio of OH^- to Y^{3+} at the sol-gel transition was approximately 0.7. This is about half of the expected ratio of 1.5 (ratio of O to Y in Y_2O_3).

However, the fact that this ratio was consistently obtained in Figures 4, 5 B and 6 makes it unlikely that it was an experimental error.

The reason for the sol-gel transition point consistently being half of that expected is most likely because when the OH^- content became too large, path *c* in Figure 3 became favourable compared with path *b*, leading to precipitation. The main discrepancy to this is in Figure 5 A, when the $[OH^-]$: $[Y^{3+}]$ ratio almost increased to 1.5. However, this is mainly due to the volume added to reach the sol-gel transition point being very small (1 mL). It was difficult to judge precisely where the transition point occurred. Further trials with concentrations below 3 mol/L of NaOH should be done to reliably determine whether the $[OH^-]$:$[Y^{3+}]$ changes from ~0.7:1.

3.2 Electroplating Process

Before Y_2O_3 nanoparticles could be added to the Ni-Cr coatings, the conditions for electroplating Ni-Cr coatings with good oxidation and wear resistance first needed to be established. The factors that affect the electroplated coating quality and Cr content are pH, temperature, Cr^{3+} content in the electrolyte and current density. From literature, the reported optimum pH value for Ni-Cr deposition is 2.5, temperature 25 ^oC, Cr^{3+} content 75 g/L and current density 160 mA/cm^2 (Xu, *et al.*, 2007). The optimum pH and temperature values were confirmed from preliminary trials. The optimum Cr^{3+} content in the bath was found to be 80 g/L, which was very close to literature. This value was found by analysing the EDS spectra of the coating cross-sections; 80 g/L of Cr^{3+} in the bath allowed the Cr content in the coating to exceed 20 wt.%, which is the minimum needed for protective chromia scale to cover the coating (Sloof, 2008). The effects of the deposition technique on the coating quality are discussed in Sections 3.2.1 and 3.2.2.

3.2.1 DC vs. Pulse Plating

Oxidation tests were done at 900 ^oC to determine the best coating technique. The effective current density here was 70 mA/cm^2. All direct current (DC) plated Ni-Cr coatings spalled off in oxidation testing at 900 ^oC. This can be seen from the negative mass gains in Figure 7. From Figure 8, there appears to be cracks running throughout the DC plated coating. According to Lin *et al.*, cracks are commonly observed on electrodeposited Cr and Cr alloy coatings. This was attributed to the unstable chromium hydrides forming and decomposing to evolve hydrogen gas. Cracks result from the large tensile stresses generated by the 15% decrease in volume when the hydrogen gas is released (Lin, Hsu & Chang, 1992). The evolution of hydrogen gas would also lead to significant porosity in the coating, which would weaken the bonds between the coating and substrate. Consequently, when thermal stresses are applied during oxidation testing, the coating would readily spall off.

It is reported that pulse plating can overcome cracking in Ni-Cr coatings (Lin, *et al.*, 1992). This involves a periodic alternation in current direction. The reverse currents cause the hydrides to decompose (Lin, *et al.*, 1992).

From the optical micrograph of the pulse plated Ni-Cr coating shown in Figure 9, it can be seen that the coating is crack-free. Also, from the preliminary oxidation test results shown in Figure 7, it can be seen that the pulse plated Ni-Cr coating remained intact throughout the oxidation test. The parabolic rate constant ($k_p = [4.9 \pm 0.6] \times 10^{-4}$ mg^2.cm^{-4}.hr^{-1}) for the pulse plated Ni-Cr was lower than that of the uncoated stainless steel ($k_p = [8 \pm 2] \times 10^{-4}$ mg^2.cm^{-4}.hr^{-1}), indicating that the pulse plated Ni-Cr coating was adherent and more protective. It can be seen that pulse plating can overcome cracking in the Ni-Cr coatings and was therefore used in all subsequent experiments.

3.2.2 The Effect of Current Density

Mechanical and oxidation properties were used to assess the effect of the applied current densities on the coating quality. From the trials with DC plating, it was found that using 160 mA/cm^2 (Section 3.2) was too high because the coatings were cracked and not adherent. On the other hand, when the current density was too low (< 50 mA/cm^2), there was no deposition. The optimum current density was found to be ~80 mA/cm^2. Based on this, three current density patterns (Table 1) were studied in detail through oxidation tests. The pulse pattern consisted of a forward period of 5 ms and reverse period of 3 ms (Lin, *et al.*, 1992).

Figure 10 shows that when the forward current density was larger than the reverse current density (Pattern C), spallation occurred, similar to DC plating. One possibility is that the driving off of hydrogen gas by the reverse pulses was inadequate, leading to a reduction in the adhesion of the coating to the substrate.

Thus, the two desirable current density patterns were those of Patterns A or B. Wear testing was used to decide on which to use since it indicates at the adhesion of the coating. Figure 11 indicates that when plating with a larger reverse current density (Pattern B), the wear resistance was larger and also higher than uncoated stainless steel.

These results were because the reverse currents have a tendency to dissolve more Ni, leading to a higher Cr composition (Lin, *et al.*, 1992). As Cr has a higher hardness than Ni, the Ni-Cr coating was harder overall.

From these studies, the optimum forward pulse current density for Ni-Cr electroplating was found to be 320 mA/cm^2, with a period of 5 ms. The optimum reverse current density was 340 mA/cm^2, with a period of 3 ms. The electrolyte composition was also developed as part of the second aim and is given in Table 2.

3.3 Comparison of Oxidation Resistance

Ni-Cr-Y_2O_3 composite coatings were produced by immersing the steel substrates in the Ni-Cr bath with Y_2O_3 sol added to it and electrodepositing the coating onto the substrates (see Section 2.). In order to fulfil the third aim, the oxidation behaviour of the Ni-Cr-Y_2O_3 coatings was compared with Ni-Cr, Ni-Cr electroplated with Y^{3+} solution in the electrolyte (Ni-Cr-Y), and Ni-Cr electroplated with 0.04 mol/L Y_2O_3 added as powder to the bath.

As the parabolic model indicates that the scale is protective, linear regression between the square of mass gain per unit area (t_s^2) and time of oxidation (t) was used to obtain the rate constants of the fitted parabolic model (Figure 12). These are given in Table 3. It can be seen that in all cases, the variability captured by the parabolic models exceeds 85% (from the Multiple-R^2 values), indicating that the parabolic model is suitable for making predictions. The p-values for the parabolic rate constants are all below 0.001, which provides very strong evidence against their being zero. Overall, these indicate that the parabolic models are suitable for the mass gains of the samples during oxidation, and the scale on all coatings were stable. Also, a lower parabolic rate constant usually indicates at an improved oxidation resistance (Young, 2008). Ni-Cr-Y has the lowest parabolic rate constant. This is in agreement with literature: adding Y improves the oxidation resistance of the alloy through the rare earth effect (Hussey, Sproule, & Graham, 1993; Whittle & Stringer, 1980). But Ni-Cr coatings with Y_2O_3 added as sol and powder both had slightly higher parabolic rate constants than Ni-Cr.

However, an important determinant of oxidation resistance is the adhesion of the scale to the coating. Adhesion is indicated by oxide scale spallation; the more scale that spalls off, the poorer the adhesion (Haynes, Pint, Porter, & Wright, 2003). The spallation results are shown in Figure 13. The fitted model for the spallation per unit area (s) of Ni-Cr was $s^2 = (8 \pm 1) \times 10^{-4} t$; for Ni-Cr deposited with Y_2O_3 powder was $s^2 = (7 \pm 2) \times 10^{-4} t$. The F-statistic p-values were both <0.001, indicating at very strong evidence against the proportionality constants being zero. The p-values for the F-statistics of linear models fitted to the spallation of Ni-Cr-Y and Ni-Cr-Y_2O_3 were both ~0.1, indicating at no evidence against spallation changing with time from zero. This indicates that the oxidation resistance of Ni-Cr-Y and Ni-Cr-Y_2O_3 coatings were significantly better than the other two coatings, due to the much lower spallation.

The improvement in oxidation resistance of Ni-Cr-Y_2O_3 composite coatings is also supported by the SEM micrographs in Figures 14 A to D. These show that the Ni-Cr, Ni-Cr electroplated with Y_2O_3 powder and Ni-Cr-Y coatings all had oxide scale with some degree of spallation. By contrast, the Ni-Cr-Y_2O_3 coating had an oxide scale that was compact with no spallation. These SEM micrographs also show that although no significant spallation of Ni-Cr-Y coatings was measured, some spallation did actually occur. This indicates that the Ni-Cr-Y_2O_3 composite coatings have better oxidation resistance than Ni-Cr-Y coatings.

Two of the main theories to explain how the rare earth effect reduces spallation are the oxide pegging model and grain refinement by the solute-drag effect (Whittle & Stringer, 1980). The most likely explanation for the reduction in spallation with the Ni-Cr-Y and Ni-Cr-Y_2O_3 coatings is grain refinement. XRD analysis showed that the oxidised samples had magnetite, chromia, $NiCr_2O_4$ and chromium-iron oxides present. But only the magnetite peaks did not overlap in the diffractograms, meaning that only these could be analysed to compare the oxide grain size of the different coatings. From Figure 15 and Table 4, it can be seen that the ~50 nm magnetite grain size on Ni-Cr is reduced by the addition of Y and even more by the addition of Y_2O_3 sol, in which the grain size is ~30 nm. Assuming that the trends in the grain size of magnetite are the same across all other crystals (especially Cr_2O_3), the Ni-Cr-Y_2O_3 composites would have formed the smallest chromia grains.

Grain refinement would be due to Y_2O_3 nanoparticles either acting as nucleation sites for grains in the scale, or due to the pinning effect of the grain boundaries, which prevents them from growing (Whittle & Stringer, 1980). The Y in Ni-Cr-Y would have oxidised to form Y_2O_3 and thereby resulted in grain refinement. But the Y_2O_3 in Ni-Cr-Y_2O_3 would have been present from the start to nucleate small grains and pin grain boundaries, leading to further grain refinement. Ni-Cr-Y_2O_3 composite coatings should therefore have better oxidation resistance than Ni-Cr-Y coatings. This is because Ni-Cr-Y_2O_3 coatings have a higher grain boundary density, which should lead to the greater relief of thermal stresses during oxidation testing.

4. Conclusions

Electroplating has been used to produce oxidation resistant Ni-Cr coatings with a fine dispersion of Y_2O_3 nanoparticles. The processing, microstructure and properties of the composite coatings were studied in detail. The main results are presented below:

Y_2O_3 nanoparticles were synthesised in sol by controlled hydrolysis and condensation. Nanoparticles of 54 ± 2 nm were formed.

It is believed that Y_2O_3 nanoparticles form by OH^- complexing with Y^{3+} through a series of hydrolysis and condensation reactions, producing Y-O-Y complexes. These produce Y_2O_3 nanoparticles after aging due to further complexing.

Pulse plating with a forward period of 5 ms and reverse period of 3 ms electrodeposited crack-free Ni-Cr coatings onto the 316 stainless steel substrate.

In studies on current density, it was found that the most wear and oxidation resistant Ni-Cr coatings occurred when the forward current density was 320 mA/cm^2 and reverse current density 340 mA/cm^2; the overall current density was 70 mA/cm^2.

Spallation results show that Ni-Cr-Y and Ni-Cr-Y_2O_3 coatings possess better oxidation resistance than Ni-Cr and Ni-Cr electroplated with Y_2O_3 powder. Results indicate that this was because of the enhanced scale plasticity due to the finely dispersed Y_2O_3 nanoparticles refining the grain size.

There is evidence to suggest that adding Y_2O_3 nanoparticles via sol improves the oxidation resistance of Ni-Cr coatings than when Y is added as an element. Extended oxidation tests need to be done to provide further support to this conclusion.

Acknowledgements

The authors would like to thank Dr. Weiwei Chen, Dr. Balan Zhu, Yongjian Yang, Dr. Michelle Dickenson, Caizhen Yao, Zendi Yang, Shanghai Wei, Steve Strover, Dr. Alec Asadov, Catherine Hobbis, Dr. Adrian Turner, Ian Yan, Peter Buchannan and Laura Liang for their help on this project.

References

Barlier, V., Bounor-Legaré, V., Boiteux, G., Davenas, J., & Léonard, D. (2008). Hydrolysis-condensation reactions of titanium alkoxides in thin films: A study of the steric hindrance effect by X-ray photoelectron spectroscopy. *Applied Surface Science*, *254*(17), 5408-5412. http://dx.doi.org/10.1016/j.apsusc.2008.02.076

Buscail, H., Caudron, E., Cueff, R., El Messki, S., Issartel, C., & Riffard, F. (2004). Effect of reactive element oxide coating on the high temperature oxidation behaviour of FeCrAl alloys. *Applied Surface Science*, 229, 233-241.

Chen, W., & Gao, W. (2010). Sol-enhanced electroplating of nanostructured Ni-TiO2 composite coatings-The effects of sol concentration on the mechanical and corrosion properties. *Electrochimica Acta*, *55*(22), 6865-6871. http://dx.doi.org/ 10.1016/j.electacta.2010.05.079

Cheng, X. (1999). *Synthesis of Nanometer-sized Yttrium Oxide Particles in Diisooctyl Sodium Sulphosuccinate (AOT)/Isooctane Reverse Micelle Solution*. (Master of Science dissertation). Virginia Polytechnic Institute and State University, Blacksburg, Virginia, USA.

U.S. Energy Information Administration. (2010). *International Energy Outlook 2010*. Washington, DC: Doeman, L. E.

Gao, W. (2011). *Materials Engineering: CHEMMAT 423* [Lecture notes]. Auckland, New Zealand: University of Auckland, Department of Chemical and Materials Engineering.

Gao, W., & Chen, W. (2009). *International Patent No.: PCT/NZ2010/000128*. Auckland, New Zealand: Auckland Uniservices Limited.

Haynes, J. A., Pint, B. A., Porter, W. D., & Wright, I. G. (2003). Comparison of Thermal Expansion and Oxidation Behavior of Various High-Temperature Coating Materials and Superalloys. *Materials at High Temperature*, 1-24.

Hussey, R. J., & Graham, M. J. (1996). The influence of reactive-element coatings on the high-temperature oxidation of pure-Cr and high-Cr-content alloys. *Oxidation of Metals*, *45*(3), 349-374. http://dx.doi.org/ 10.1007/bf01046989

Hussey, R. J., Sproule, G. I., & Graham, M. J. (1993). The effect of reactive element coatings on the oxidation behaviour of pure Cr and high Cr-content alloys at 900℃. *Journal De Physique IV*, 3, 241-246.

Lin, K. L., Hsu, C. J., Hsu, I. M., & Chang, J. T. (1992). Electroplating of Ni-Cr on Steel with Pulse Plating. *JMEPEG*, 1, 359-362.

Rahman, A., Chawla, V., Jayaganthan, R., Chandra, R., & Ambardar, R. (2010). Evaluation of High Temperature Oxidation Behaviour of Nanostructured Cr/Co–Al Coatings. *Oxidation of Metals*, *74*(5), 341-358. http://dx.doi.org/ 10.1007/s11085-010-9217-3

Seal, C. (2011). *Advanced Materials Characterisation: CHEMMAT 724* [Lecture notes]. Auckland, New Zealand: University of Auckland, Department of Chemical and Materials Engineering.

Sloof, W. (2008). Self Healing in Coatings at High Temperatures. In S. Zwaag (Ed.). *Self Healing Materials, 100*, 309-321. Dordrecht, Netherlands: Springer Netherlands.

Smith, J. M., Van Ness, H. C., & Abbott, M. M. (2005). *Introduction to Chemical Engineering Thermodynamics* (7th ed.). New York, NY: McGraw-Hill. (Original work published 1949).

Trinidade, V., Christ, H.-J., & Krupp, U. (2010). Grain-Size Effects on the High-Temperature Oxidation Behaviour of Chromium Steels. *Oxidation of Metals*, *73*(5), 551-563. http://dx.doi.org/10.1007/s11085-010-9192-8

Wang, F., Wang, W., Yu, P., & Zhu, S. (2008). Cyclic Oxidation Behavior of Sputtered Nanocrystalline Coating with Yttrium Additions in Air. *Materials Science Forum*, *595-598*, 1163-1171.

Whittle, D. P., & Stringer, J. (1980). Improvements in High Temperature Oxidation Resistance by Additions of Reactive Elements or Oxide Dispersions. *Philosophical Transactions of the Royal Society of London. Series A, Mathematical and Physical Sciences*, *295*(1413), 309-329.

Xu, L. j., Gong, Z. q., Tang, J. x., He, Q. g., He, N. y., & Du, J. j. (2007). Ni-Cr alloy electrodepositing technology on Fe substrate and coating performance. *Journal of Central South University of Technology*, *14*(2), 181-185. http://dx.doi.org/ 10.1007/s11771-007-0036-x

Young, D. J. (Ed.). (2008). *High Temperature Oxidation and Corrosion of Metals* (1st ed.). Oxford, UK: Elsevier.

Table 1. Current density patterns studied in oxidation testing

Bath	i_f (mA/cm²)	i_r (mA/cm²)	$i_{effective}$ (mA/cm²)
Pattern A	320	320	80
Pattern B	320	340	70
Pattern C	360	320	100

Table 1 specifies the forward (i_f), reverse (i_r) and effective ($i_{effective}$) current densities for the various current patterns that were used to electroplate Ni-Cr. The samples for each pattern were oxidation tested at 900 ℃ to determine which pattern to use.

Table 2. Final electrolyte composition for Ni-Cr plating

Compound added to Electrolyte	Mass added (g)	Concentration (g/L)	Concentration (mol/L)
$NiSO_4.6H_2O$	4	45	0.17
$NiCl_2.6H_2O$	3.6	41	0.17
$CrCl_3.6H_2O$	7.2	80	0.31
H_3BO_3	4	45	0.74
$NaC_{12}H_{25}SO_4$	0.016	0.18	0.0006
***NaF**	0.24	2.7	0.065
****$C_2H_5NO_2$**	5.07	58	0.77

*NaF was added as a brightener to reduce the density of carbides on the surface of the coatings and thereby reduce the darkness of the coatings.

**Glycine was added as a complexing agent to allow chromium deposition.

The final volume of the electrolyte was 88 mL: 80 mL distilled water, 8 mL of 2 g/L sodium dodecyl sulfate.

Table 3. Comparison of parabolic rate constants and goodness of fit of parabolic models to mass gain curves

Change to Coating	k_p ($mg^2.cm^{-4}.hr^{-1}$)	k_p ($mg^2.cm^{-4}.hr^{-1}$)	Variability captured by model	p-value for k_p
Uncoated 316 Stainless Steel	0.0008	0.0002	92%	9.6×10^{-6}
Ni-Cr	0.00049	0.00006	96%	1.7×10^{-10}
Ni-Cr-Y	0.00036	0.00007	86%	1.8×10^{-10}
Ni-Cr with 0.04 M Y_2O_3 Powder	0.0008	0.0001	92%	2.8×10^{-8}
Ni-Cr-Y_2O_3	0.0006	0.0001	86%	1.8×10^{-10}

In Table 3, the parabolic rate constants were determined by linear regression between the square of mass gain and time of oxidation. The uncertainties are two standard deviations for the rate constant. The variability captured by the model refers to the Multiple-R^2 from the F-test, from which the p-values were also obtained.

Table 4. Calculation of magnetite grain size using line broadening

Coating	$2\theta/^o$	FWHM/^{o}	τ/nm
Ni-Cr	62.51	62.51	49
Ni-Cr-Y	62.31	62.31	46
Ni-Cr with powder	42.93	42.93	56
Ni-Cr-Y_2O_3	62.20	62.20	30

In Table 4, the FWHM was obtained from Figure 14 from the {440} peaks of Magnetite. However, the FWHM of Ni-Cr with powder needed to be obtained from the {400} peak, as the {440} peak had too much overlap with nickel chromium oxide for that particular sample. The Miller indices were determined using Bragg's law and the magnetite have a cubic unit cell and lattice parameter of 8.44 Å. The line broadening due to the diffractometer was found to be 0.137^o. Scherrer's constant was taken as 0.9.

ISSN 1927-0585 E-ISSN 1927-0593

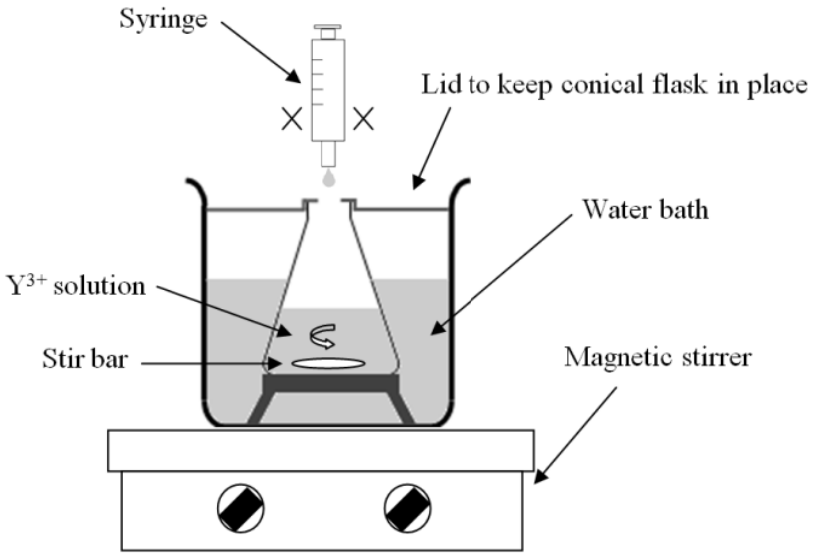

Figure 1. Schematic showing the setup used for nanoparticle synthesis by the sol-gel method

The key features of the design shown in Figure 1 include the water bath to maintain low temperatures, which prevents the nanoparticles from aging. There is also agitation to break apart any gels, and a low droplet rate to avoid instant gelification.

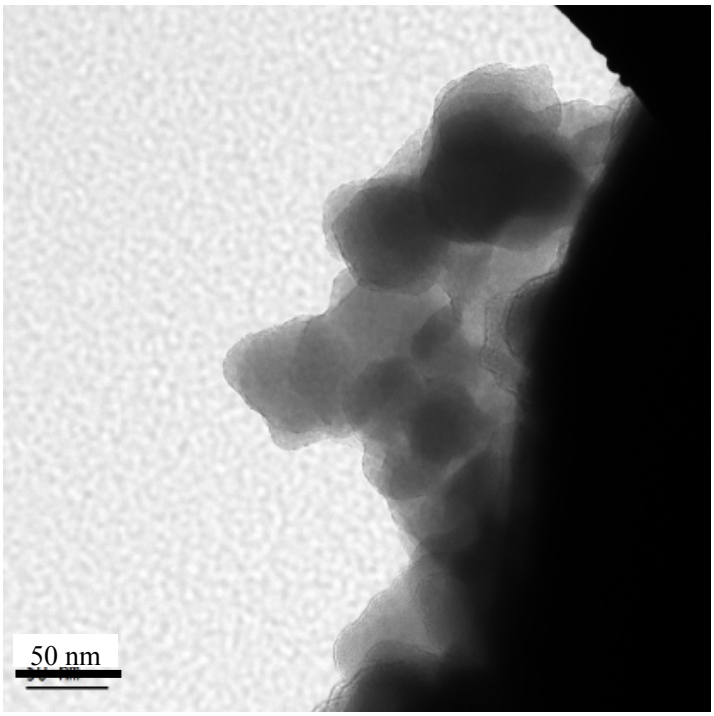

Figure 2. TEM micrographs of Y_2O_3 from sol

The particle size was determined by analysing the micrograph in Figure 2. In Figure 2, it can be seen that are distinct spheres that are transparent. This indicates at agglomerated particles that are smaller than 100 nm, and through which the electron beam in the TEM would penetrate. The dark, opaque surface the particles are agglomerated onto is one of the strands of the copper mesh that the yttria sol was dried onto.

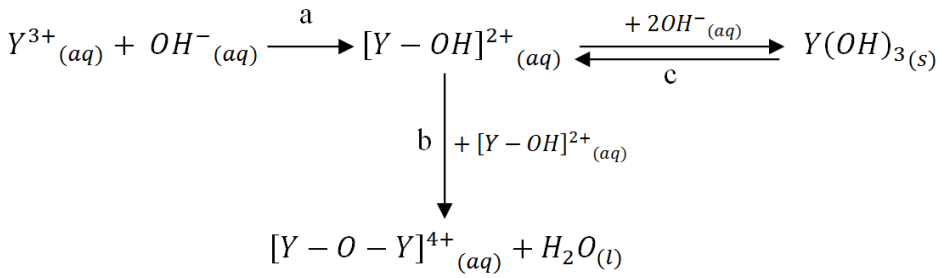

Figure 3. Sol-gel reaction pathways for Y^{3+} exposed to OH^-

Figure 3 presents the suggested reaction pathways. Pathway *a* is hydrolysis of Y^{3+} by OH^-. Pathway *b* is condensation (oxolation) between two Y-OH complexes to form the Y-O-Y complex. It is believed that this complexes further with ageing to form Y_2O_3. Pathway *c* occurs when excess OH^- is present, such as when the droplet rate of OH^- is too high; precipitation of $Y(OH)_3$ occurs, which is undesirable for nanoparticle synthesis.

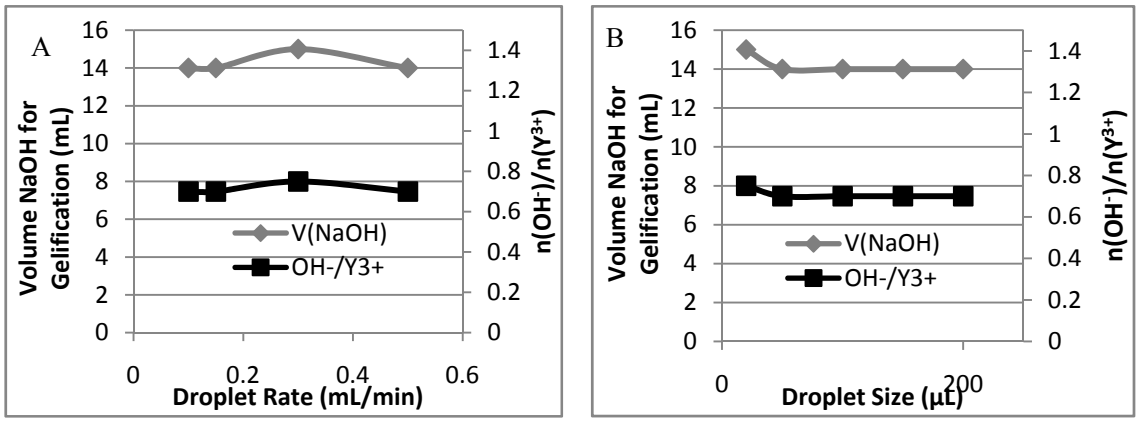

Figure 4. Volume of NaOH added to reach sol-gel transition and ratio of $n(OH^-)$ at gelification to $n(Y^{3+})$ in solution as a function of rate of OH- addition (A) and size of droplets (B)

Figure 4 shows that the volume of 0.2 mol/L NaOH added to gelify 20 mL of 0.2 mol/L Y^{3+} is independent of droplet rate or droplet size, as the ratio of the amount of OH^- added at gelification to the amount of Y^{3+} present in the solution is approximately constant in both cases.

ISSN 1927-0585 E-ISSN 1927-0593

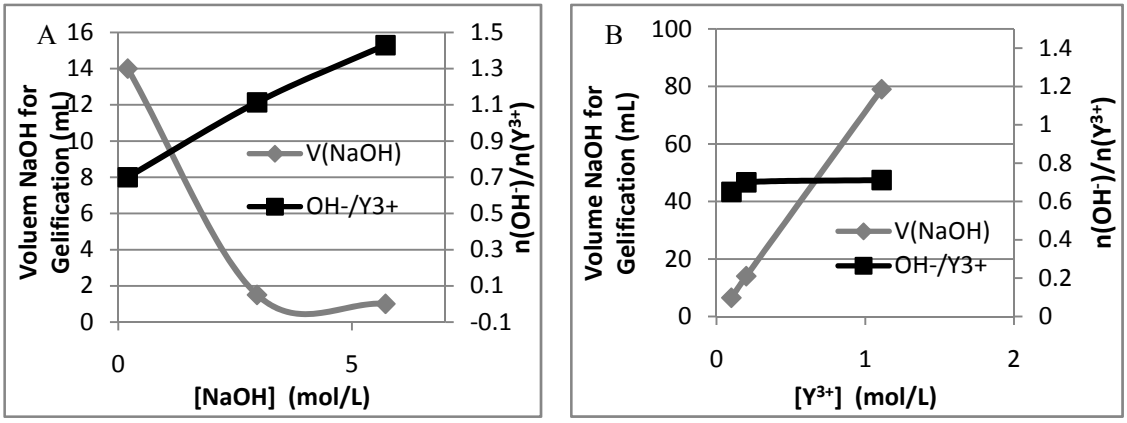

Figure 5. Volume of NaOH added to reach sol-gel transition and ratio of amount of NaOH added at transition point to the amount of Y^{3+} in the solution as a function of the concentration of NaOH added to the solution (A) and concentration of Y^{3+} in the solution (B)

Figure 5 shows that the volume of NaOH needed to gelify 20 mL of Y^{3+} decreases with the concentration of NaOH but increases with the concentration of Y^{3+}. However, the ratio of the amount of OH^- added at gelification to the amount of Y^{3+} present originally is independent of $[Y^{3+}]$, but increases with [NaOH].

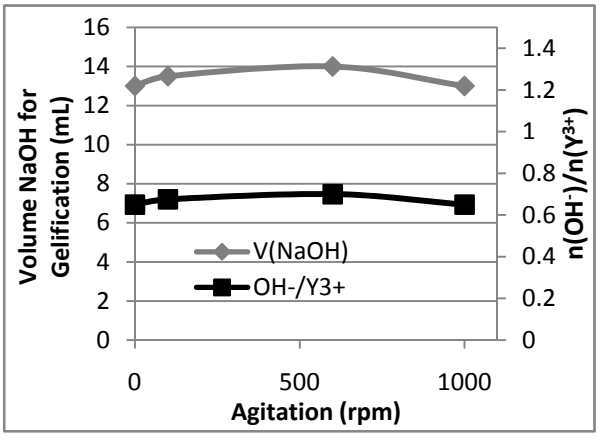

Figure 6. Volume of NaOH added to reach sol-gel transition and ratio of amount of NaOH added at the transition point to the amount of Y^{3+} in the solution as a function of agitation of the solution

Figure 6 shows that both the volume of 0.2 mol/L NaOH needed to gelify 20 mL of 0.2 mol/L Y^{3+} is independent of agitation, as the ratio of the amount of OH^- added at gelification to the amount of Y^{3+} originally present is approximately constant.

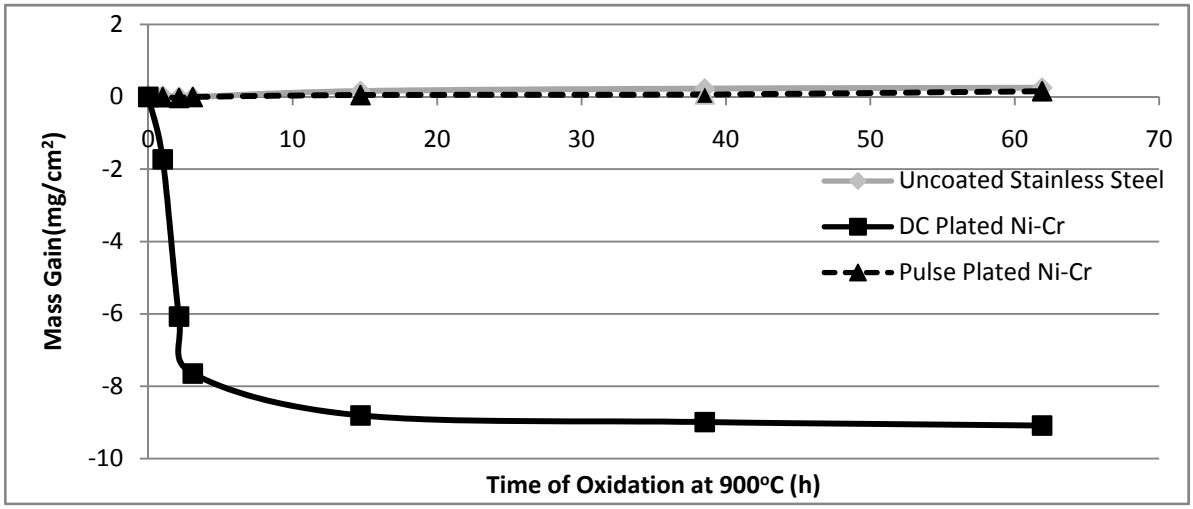

Figure 7. Mass gain of uncoated stainless steel, compared with DC and pulse plated Ni-Cr Coating

Figure 7 shows how the mass gain of DC plated Ni-Cr is significantly negative. This indicates at the spallation of the coating and scale from the substrate. The pulse plated Ni-Cr has positive mass gain, indicating that the Ni-Cr is adherent. Also, the Ni-Cr has approximately half the mass gain of uncoated stainless steel, indicating at improved oxidation resistance.

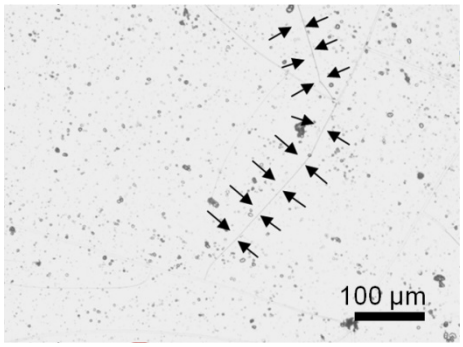

Figure 8. Optical micrograph with arrows pointing at the crack running across the DC plated Ni-Cr coating

Figure 8 shows that the DC plated Ni-Cr coatings tended to have cracks running through them. One of these is indicated by the black arrows.

 ISSN 1927-0585 E-ISSN 1927-0593

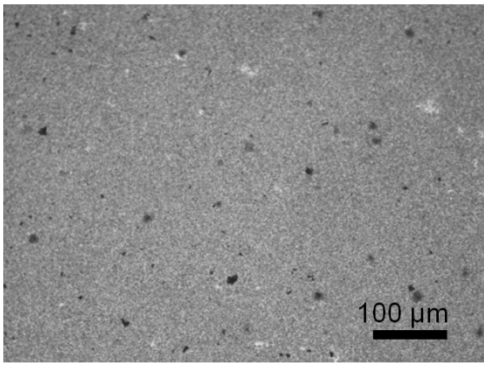

Figure 9. Optical micrograph showing the uniform and compact structure of pulse plated Ni-Cr

Figure 9 shows that with pulse plating, no cracks could be detected from optical micrographs take at 20 times magnification on the objective lens.

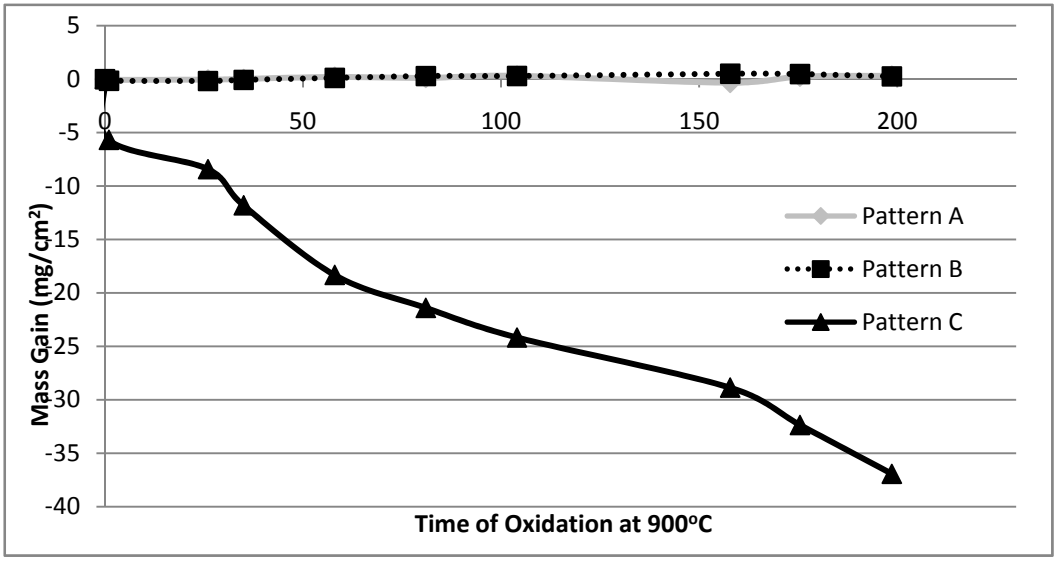

Figure 10. Oxidation kinetics of the three studied current density patterns for pulse plating

Figure 10 shows that the mass gain of Ni-Cr pulse plated by Pattern C is significantly negative, indicating at significant spallation. But Ni-Cr pulse plated by both Pattern A and B have positive mass gains, indicating at adherent coatings.

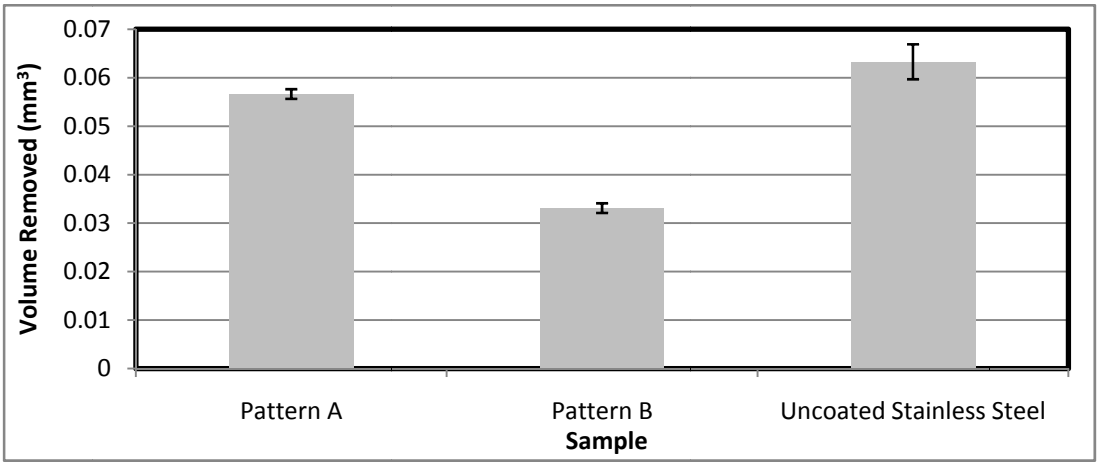

Figure 11. Wear resistance of Ni-Cr pulse electroplated with different current patterns compared with uncoated stainless steel

Figure 11 shows how the mass loss of Ni-Cr coatings pulsed plated by Pattern B have the lowest volume removed in the wear tests. This indicates at Ni-Cr of Pattern B having the highest wear resistance.

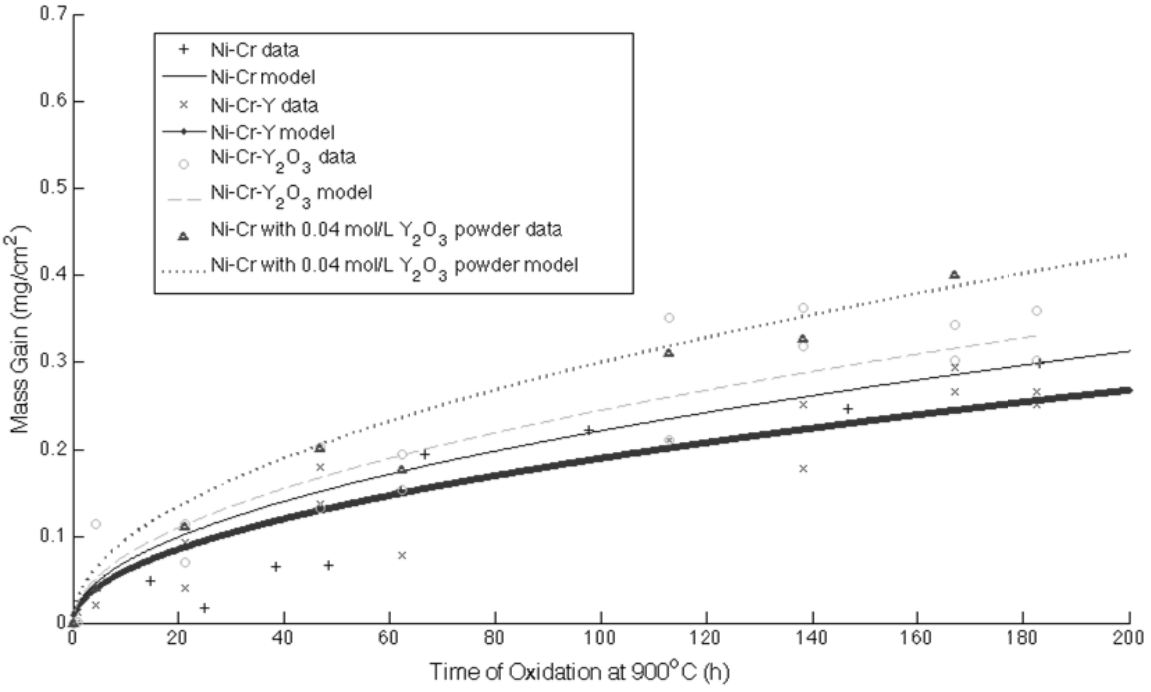

Figure 12. Comparison of mass gain (t_s) of Ni-Cr(-), Ni-Cr-Y (-.-), Ni-Cr-Y (- -), and Ni-Cr electroplated with 0.04 mol/L Y_2O_3 powder (...) in the bath

Figure 12 gives a comparison of the mass gain curves of the four types of coatings oxidation tested at 900℃ for 200 hours.

 ISSN 1927-0585 E-ISSN 1927-0593

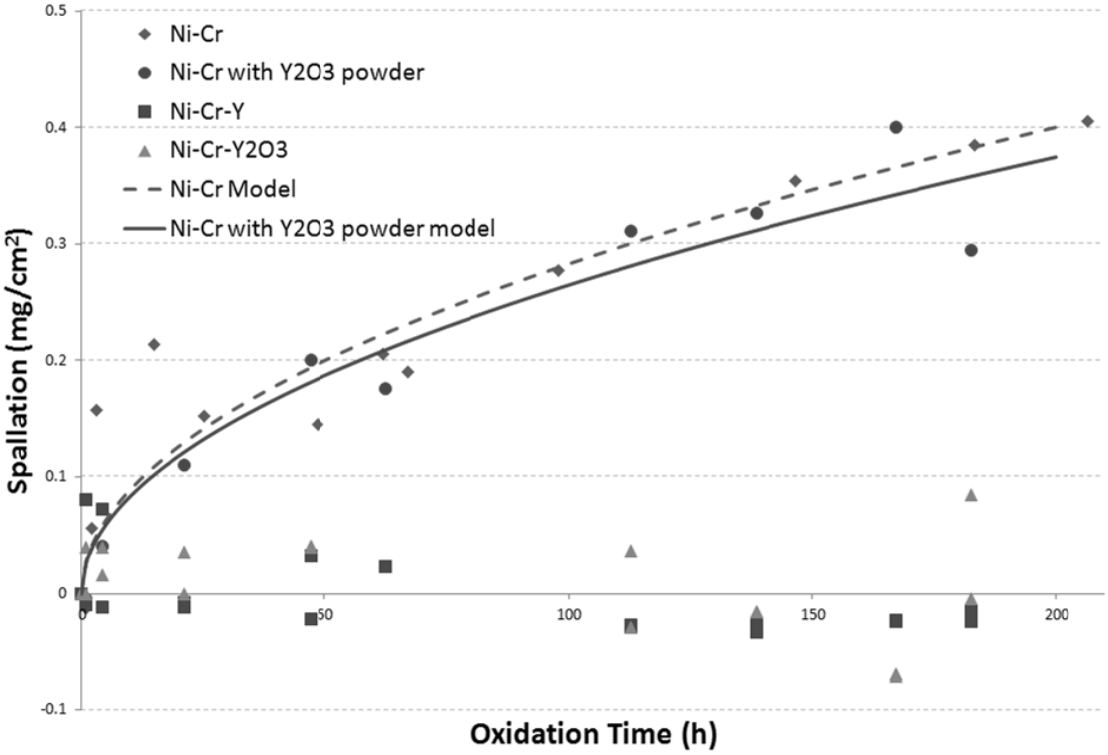

Figure 13. Spallation curves of Ni-Cr, Ni-Cr-Y, Ni-Cr-Y_2O_3, and Ni-Cr with Y_2O_3 powder added

Figure 13 compares the spallation of the four types of coatings. Both Ni-Cr and Ni-Cr with Y_2O_3 powder had similar spallation curves (which appeared to have similar shapes as the parabolic rate law), whereas the Ni-Cr-Y and Ni-Cr-Y_2O_3 coatings had almost no spallation.

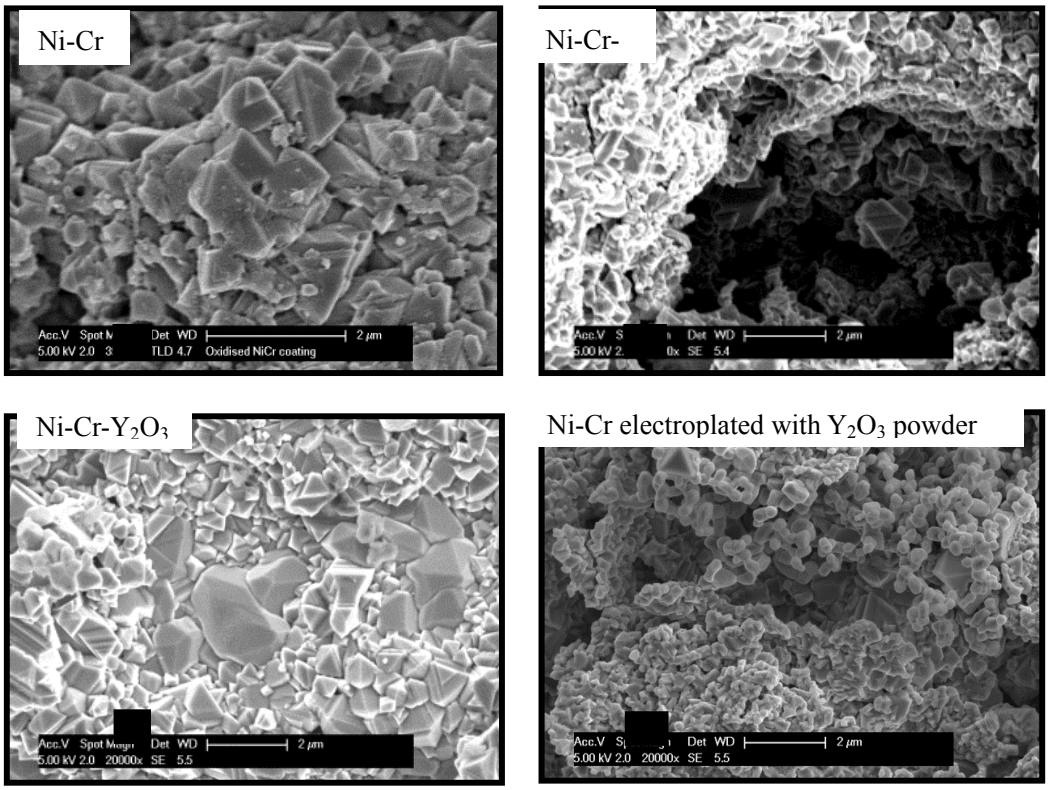

Figure 14. SEM/SE images of the oxide scale of Ni-Cr (A), Ni-Cr-Y (B), Ni-Cr-Y_2O_3 (C), Ni-Cr with Y_2O_3 powder (D)

Figure 14 shows the surface morphology of the oxide scale of all four different types of coatings. It can be seen that the Ni-Cr-Y_2O_3 composite coatings had an oxide scale that was compact, without any evidence of spallation. By contrast, all of the three other types of coatings show distinctive signs of the scale spalling away. This indicates that the Ni-Cr-Y_2O_3 composite coatings would have had the best oxidation resistance.

 ISSN 1927-0585 E-ISSN 1927-0593

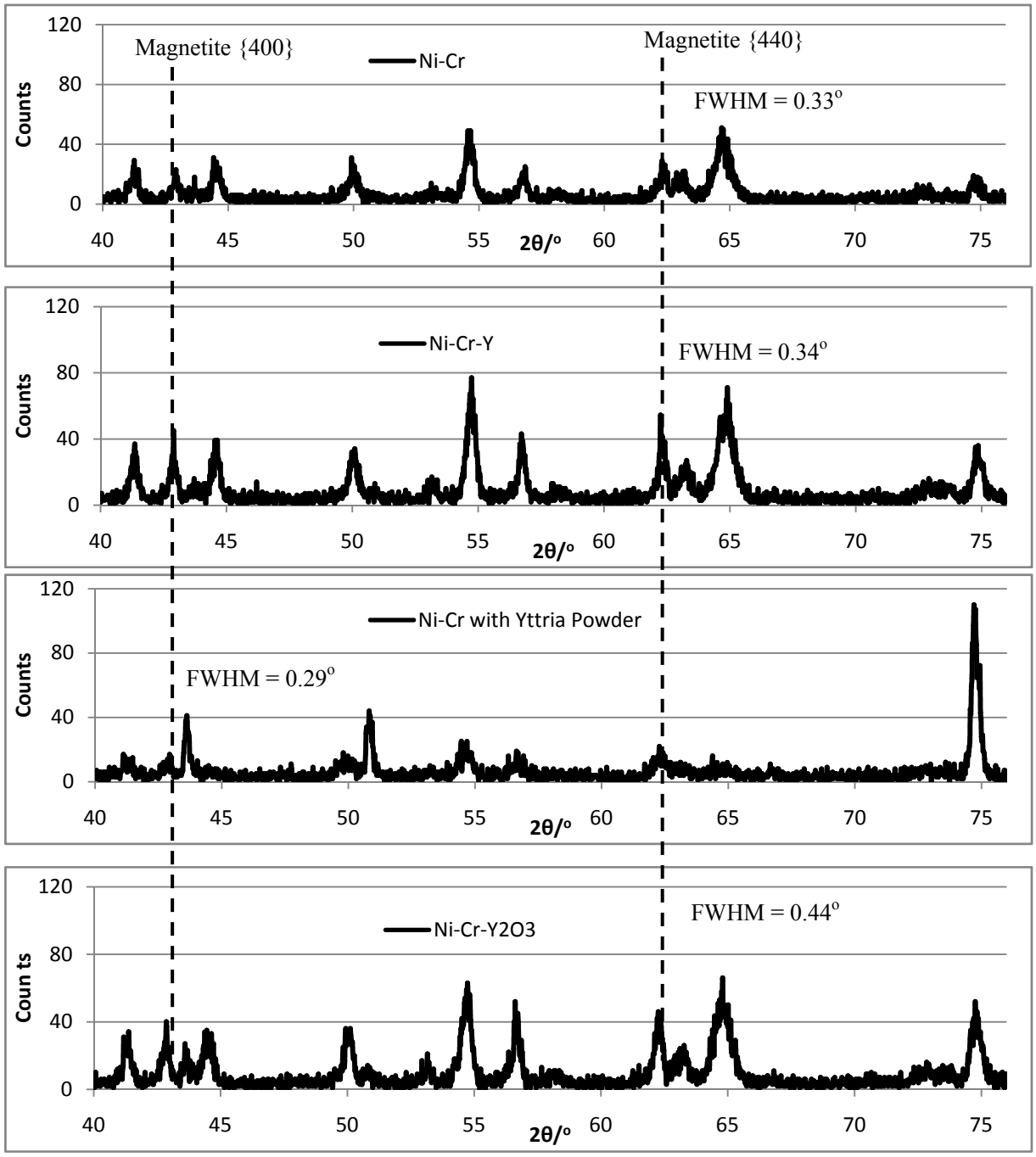

Figure 15. XRD diffractograms of oxidised coatings

Figure 15 compares the diffractograms obtained from all of the four types of coatings. The magnetite {440} peak was used for determining grain size by using the Scherrer equation. But, the magnetite {400} peak needed to be used for the Ni-Cr coating deposited with yttria powder, due its magnetite {440} peak appearing to have been broadened by overlap with nickel chromium oxide